Estuarine, Coastal and Shelf Science 190 (2017) 69–79

Contents lists available at ScienceDirect

Estuarine, Coastal and Shelf Science

journal homepage: www.elsevier.com/locate/ecss

Dynamics of sediment disturbance by periodic artificial discharges from the world's largest tidal power plant

J.W. Kim, H.K. Ha*, S.B. Woo

Department of Ocean Sciences, Inha University, Incheon 22212, South Korea

ARTICLE INFO

Article history:
Received 1 December 2016
Received in revised form
21 March 2017
Accepted 28 March 2017
Available online 30 March 2017

Keywords:
Artificial discharge
Spring and neap tides
Ebb and flood tides
Suspended sediment concentration
Vortex
Sihwa tidal power plant

ABSTRACT

To investigate the dynamics of sediment disturbance near the world's largest Sihwa tidal power plant (TPP), two mooring observations have been conducted. The mooring results show that current velocity and suspended sediment concentration (SSC) were significantly disturbed over various time scales. On the short-term (flood–ebb) time scale, resuspension of bottom sediment is mainly controlled by the strong jet-flow (>2 m s^{-1}) and resulting anticlockwise rotating vortex associated with the artificial discharge. During ebb phase, the strong flow resulted in suspension of high-concentration near-bed sediment and seaward transport of the suspended sediment. After turning to flood phase, the vortex produced secondary SSC peaks, transporting the suspended sediment toward the Sihwa TPP. The most active suspension of bed sediment predominantly occurred during 1–2 h immediately after the start of artificial discharge. For the fortnightly (spring–neap) time scale, SSC during spring tide was approximately 2–5 times higher than that during neap tide. During the combined period of ebb and spring tides, in particular, the periodic artificial discharge can enhance the responses of SSC in the vicinity of Sihwa TPP.

© 2017 Elsevier Ltd. All rights reserved.

1. Introduction

As a future source of marine renewable and sustainable energy, tidal energy has attracted considerable interest in coastal regions (Rourke et al., 2010a; Tolón-Becerra et al., 2011). Numerous tidal power plants (TPPs) have been constructed, of which the plant at La Rance is a renowned example, and potential candidate sites are still being proposed and evaluated to meet the continued increase in society's electricity demands (Charlier and Finkl, 2009; Rourke et al., 2010a). Energy exploitation by a TPP is an infinite energy source which can produce electricity based on the impounded surface area and the square of the water level difference inside and outside of the seawall (Rourke et al., 2010b; Angeloudis and Falconer, 2017, in press). Despite the economic benefits, it has been reported that anthropogenic activities associated with the construction and operation of a TPP could create serious problems in the associated hydrodynamics and sedimentary processes (Kirby, 2010; Xia et al., 2010; Neill et al., 2012; Ahmadian et al., 2014; Ramos et al., 2014; Zhou et al., 2014).

Lake Sihwa, an artificial lake formed by a seawall, is located in the southern part of Gyeonggi Bay, on the west coast of South Korea (Fig. 1). After the construction of the seawall, leading to the restriction of free exchange between freshwater discharge and seawater, sedimentation and water pollution worsened with continuous point and non-point contaminant inputs from agricultural and industrial wastes (Han and Park, 1999; Li et al., 2004; Rostkowski et al., 2006). Serious pollution by heavy metals and toxic organic contamination of bed sediment has been reported (Khim et al., 1999; Yoo et al., 2008; Oh et al., 2010; Choi et al., 2011; Ra et al., 2011). To solve such problems, desalination of Lake Sihwa was abandoned in December 2000. Instead, the government decided to construct the Sihwa TPP in the middle of the seawall for tidal power generation and water quality improvement. Lee et al. (2014) mentioned that the water quality can be locally improved by the increase of seawater circulation associated with operation of TPP. Because the Sihwa area has a peak spring tidal range of about 8 m, it has been considered for many years an excellent site for electricity generation. At this time, it is the largest TPP in the world among the operating tidal power stations in terms of power capacity. The total power output capacity is about 254 MW (Bae et al., 2010). Power is generated only during flood phase, when the tidal current flows from the sea into the enclosed basin of Lake Sihwa.

* Corresponding author.
E-mail addresses: hahk@inha.ac.kr, hokyung.ha@gmail.com (H.K. Ha).

http://dx.doi.org/10.1016/j.ecss.2017.03.029
0272-7714/© 2017 Elsevier Ltd. All rights reserved.

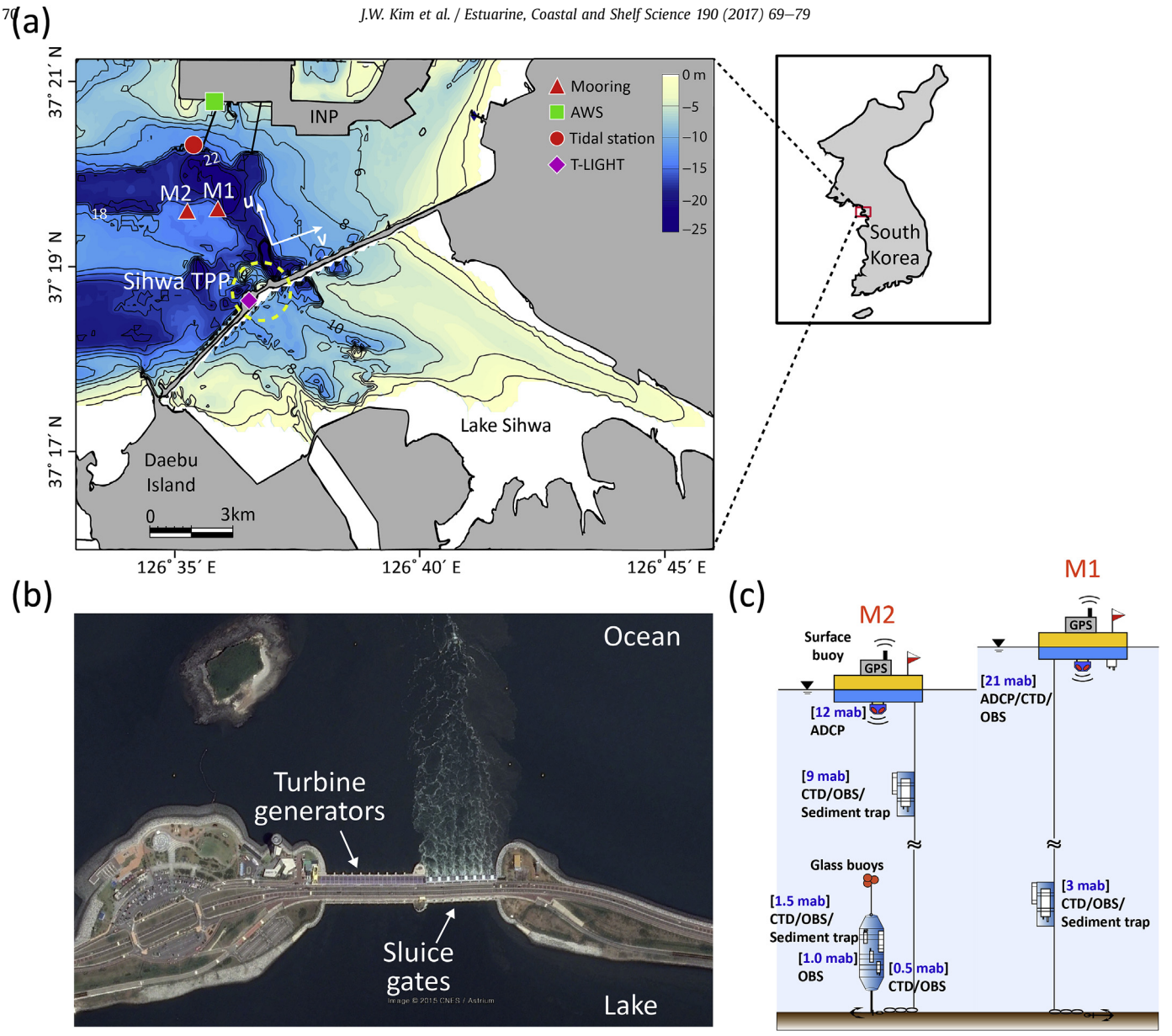


Fig. 1. (a) Map showing Lake Sihwa and the adjacent region. Hydrographic data was collected at two mooring sites (red triangles, M1 and M2), atmospheric data was collected at the AWS (green square), tide data was collected at the Songdo tidal station (red circle) by the Korea Hydrographic and Oceanographic Agency, and discharge data was collected at the T-LIGHT station (purple diamond). ADCP velocities were rotated +9.21° as shown, to represent along (u) and across (v) channel components. The along-channel velocity is parallel with the axis of the artificial discharge. INP denotes Incheon New Port. (b) Strong jet-flow of artificial discharge captured by satellite (source: Google Earth), and (c) conceptual design for moorings M1 and M2 (not to scale). (For interpretation of the references to colour in this figure legend, the reader is referred to the web version of this article.)

During ebb phase, the outgoing water passes through the sluice gate without generating any power. Such a repetition of inflow (flood) and outflow (artificial ebb discharge) caused salient changes in the hydrodynamics and sedimentary processes (Susaya et al., 2011; Kang et al., 2013). In particular, the strong artificial discharge could endanger ship traffic moving along the navigation channel in front of the Sihwa TPP.

To date, most studies for Sihwa TPP have primarily dealt with the biochemical processes associated with metals and toxic organic contamination and with ecological disturbance of benthic organisms within Lake Sihwa (e.g., Baek et al., 2011; Ra et al., 2011). A few studies, nonetheless, have attempted to investigate hydrodynamics and suspended sediment transport (e.g., Bae et al., 2010). In order to understand disturbed sediment transport processes during its operation, two in-situ moorings were installed in front of the Sihwa TPP. The primary goal of this study is to examine the effects of

Table 1
Setup details and SSC responses of the two mooring systems.

	M1	M2
ADCP		
Bin size (m)	0.50	0.25
Ping interval (sec)	0.2	1
Burst interval (min)	10	30
Deployment depth (mab)	21	12
Blanking distance (m)	0.88	0.50
CTD and OBS		
Sampling rate (Hz)	4	4
Sampling interval (min)	2	2
Deployment depths (mab)	2 levels (21 and 3)	4 levels (9, 1.5, 1.0 and 0.5)
Mean SSC_{ADCP} (mg l^{-1})		
Spring tides	27.93	25.77
Neap tides	5.73	13.46

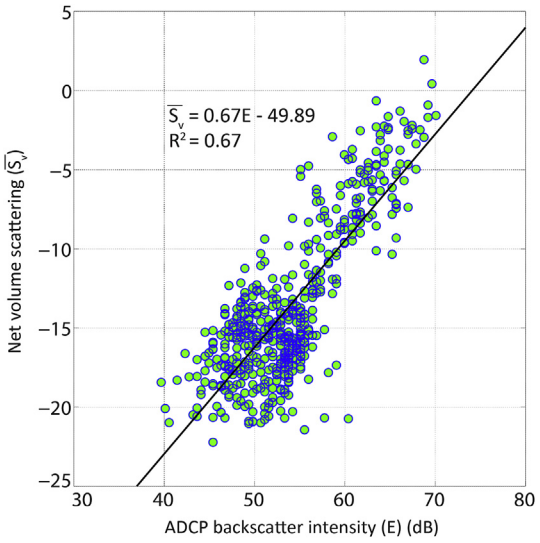


Fig. 2. Linear regression between net volume scattering and ADCP backscatter intensity.

periodic artificial discharge on the variations in velocity and suspended sediment concentration (SSC) under short-term (flood–ebb) and fortnightly (spring–neap) time scales.

2. Materials and methods

2.1. Moorings and data collection

The mooring systems were installed for the purpose of understanding the vertical and temporal variations of SSC at two stations M1 (37°19′37.20″N, 126°35′49.20″E) and M2 (37°19′36.57″N, 126°35′16.85″E), about 2.0 and 2.6 km away from the Sihwa TPP, respectively (Fig. 1). The respective mean water depths were 22 and 13 m. Mooring M1 was deployed during the period March 9 to April 15, 2013, and mooring M2 during the period November 1 to 18, 2014. Each mooring system was equipped with a 600-kHz acoustic Doppler current profiler (ADCP) (RDI, WorkHorse Sentinel), Conductivity-Temperature-Depth (CTD) sensors (RBR, XR-420 and Concerto; Idronaut, Ocean Seven 304 Plus), and an optical backscatter (OBS) sensor (Seapoint, Turbidity Meter), which were used to measure velocity profiles, temperature, salinity and turbidity, respectively (Table 1).

The downward-looking ADCP was mounted in a surface buoy, 21 [12] m above bottom (mab) for M1 [M2], respectively (Fig. 1c). Hereafter, numbers in square brackets are for M2. Time series of velocities and acoustic backscatter intensities were recorded using bin sizes of 0.50 [0.25] m, blanking distances of 0.88 [0.50] m and ambiguity velocities of 1.75 m s^{-1}. The ADCP at M1 recorded ensembles every 10 min continuously, each ensemble consisting of an average of 210 pings. The ADCP at M2 recorded every 30 min with ensemble averages of 60 pings. The ADCP transducers were located

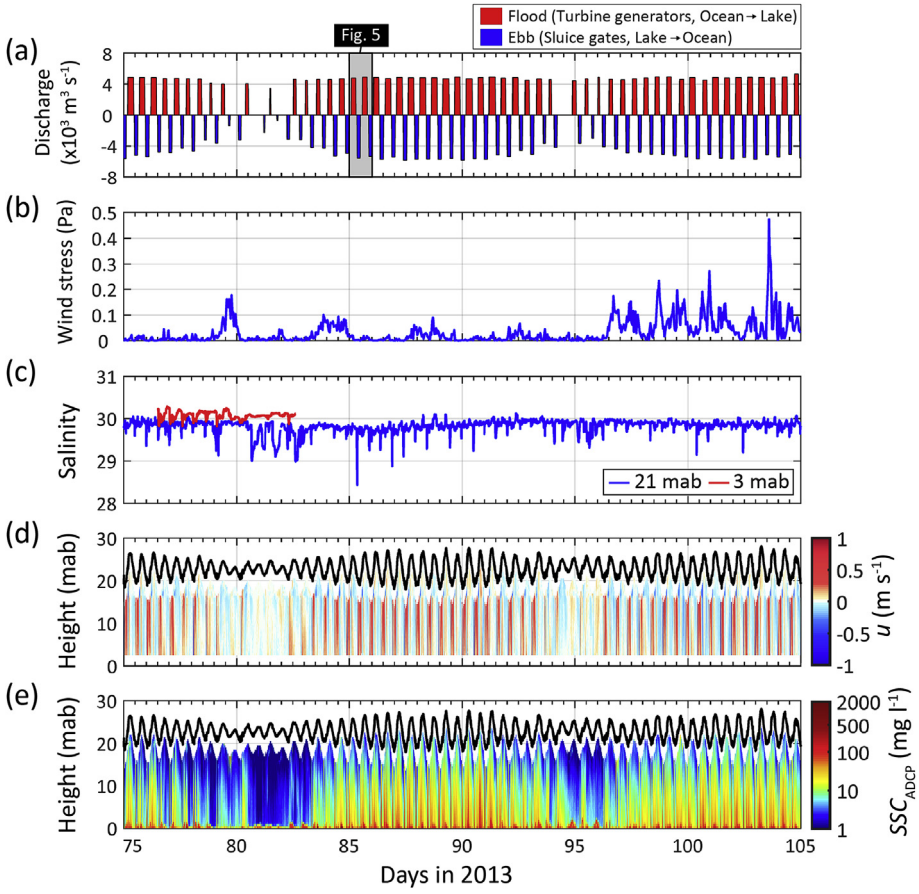


Fig. 3. Time series data from mooring M1 in 2013: (a) artificial discharge, (b) wind stress, (c) salinities at two levels, (d) along-channel velocity, and (e) SSC_{ADCP}. Thick black lines in Fig. 3d and e indicate water height.

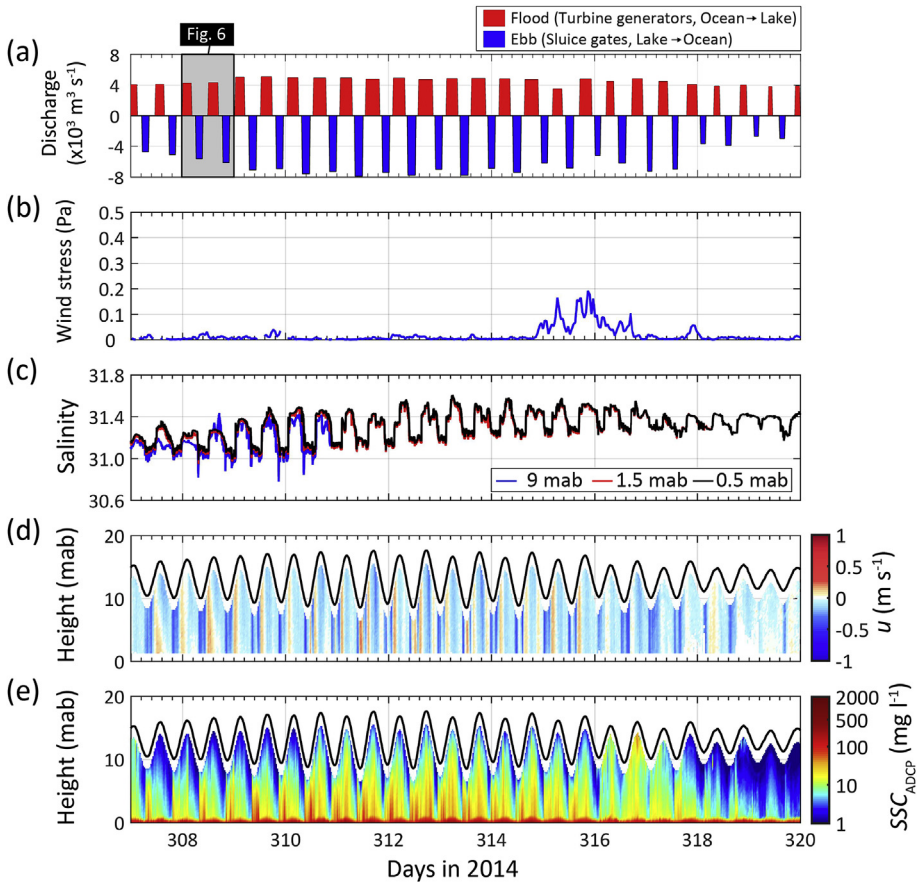


Fig. 4. Time series data from mooring M2 in 2014: (a) artificial discharge, (b) wind stress, (c) salinities at three levels, (d) along-channel velocity, and (e) SSC_{ADCP}. Thick black lines in Fig. 4d and e indicate water height.

approximately 1.0 m below the surface. The first bin was at a depth of about 2.38 [1.75] m, accounting for the blanking distance of the ADCP transducer. Due to the down-looking setup of the ADCP mounted in a surface buoy, the number of total bins was continuously varied by the changing water surface elevation over tidal cycles. The location of each bin was, therefore, rearranged based on the location of the last (near-bed) bin showing the strongest signal intensity. In the post-processing, velocity coordinates were rotated +9.21° to provide along (u) and across (v) channel components (see Fig. 1a). The along-channel velocity is parallel with the axis of the artificial discharge. Positive and negative along-channel velocities indicate northwestward and southeastward flows, respectively.

At M1, two sets of CTDs and OBSs were installed to measure the variation of temperature, salinity, and turbidity at 21 and 3 mab. At M2, a single CTD and OBS was mounted on the frame at 9.0 mab; in addition two CTDs were installed at 1.5 and 0.5 mab, and three OBSs were installed at 1.5, 1.0 and 0.5 mab (Fig. 1c). Details of the setup and configuration of the mooring systems during the two field campaigns are summarized in Table 1.

The Sihwa TPP artificial discharge was measured at the T-LIGHT station (purple diamond in Fig. 1a) operated by the Korea Water Resources Corporation (http://tlight.kwater.or.kr). Due to the hyper-tidal (mean tidal range: >6.0 m) character of the study area, mean spring and neap tidal ranges measured at the Songdo tidal station (red circle in Fig. 1a) are approximately 7.70 and 3.30 m, respectively. Daily wind velocity data was obtained at 10 m elevation from an automatic weather system (AWS) (green square in Fig. 1a). Assuming that the relationship between wind and wave is linear, the wind shear stress was estimated using the equation from Wu (1980) in which the wind coefficient increases linearly with the wind speed.

2.2. Inversion of acoustic backscatter intensity to SSC

Using a Niskin water sampler, in-situ water samples were taken to enable inversion of ADCP backscatter intensity to obtain SSC. The water sample volumes (0.7–1.0 l) were filtered by a pre-weighed and pre-dried GF/F filter (0.7 μm). The filters were oven-dried (100 °C) for 24 h. Grain size data was collected by sediment traps near the surface and bottom at M1 and M2. The M1 sediments consisted of very fine sand ($d_{50} \approx 101$ μm) and coarse sand ($d_{50} \approx 566$ μm) at the surface and bottom, respectively. In contrast, the M2 sediments consisted of coarse silt ($d_{50} \approx 33$ μm) at the bottom; M2 grain size data at the surface was not available due to unexpected sediment loss.

The acoustic backscatter calibration was performed with the modified sonar equation of Deines (1999) and Ha et al. (2011), including sound attenuation by the suspended sediment. The equation can be simplified as follows:

$$\overline{S_v} = K_c E + C^{'}, \quad (1)$$

where $\overline{S_v} = 10\cdot\log(SSC)\text{-}2(\alpha_w+\alpha_s)R\text{-}10\cdot\log(R^2)$ is the net volume scattering, E is the acoustic backscatter intensity, R is the range between transducer and measurement volume, α_w and α_s are sound

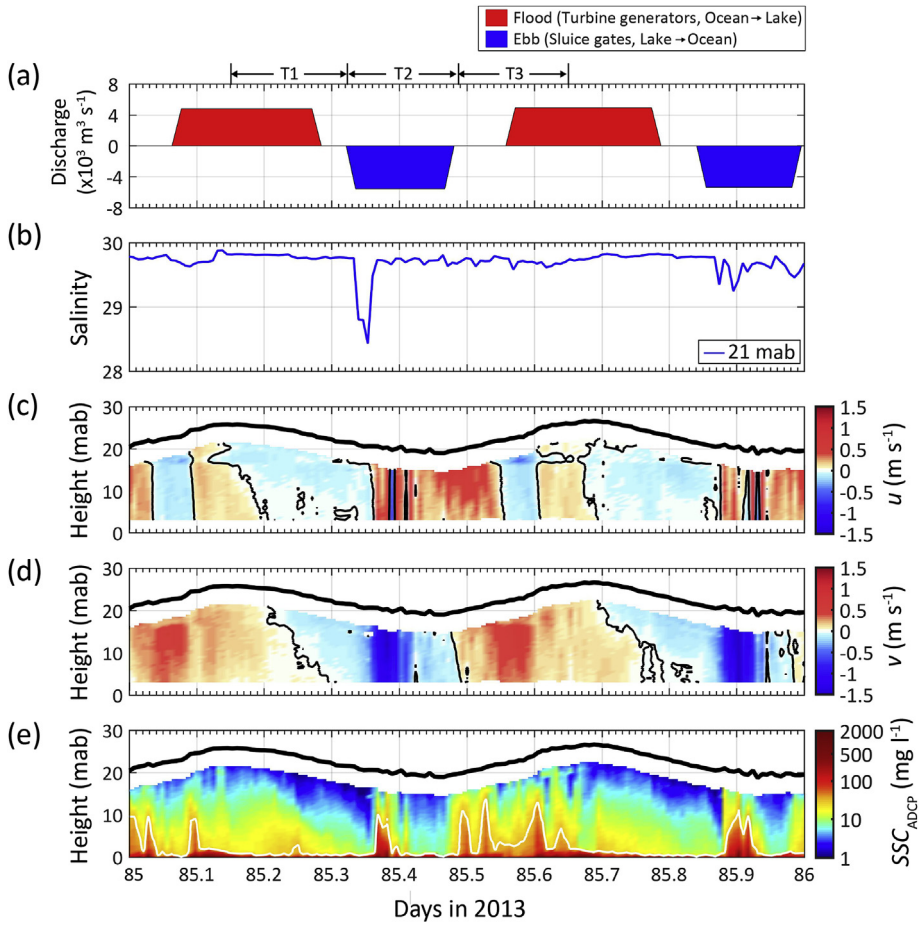


Fig. 5. Hydrodynamics and sediment dynamics at mooring M1 (for the selected time window, see Fig. 3): (a) discharge, (b) salinity, (c) along-channel velocity, (d) across-channel velocity, and (e) SSC_{ADCP}. Thick and thin black lines indicate water height (Fig. 5c, d and e) and zero velocity (Fig. 5c and d), respectively. The near-bed white line in Fig. 5e indicates 30 mg l^{-1}, used as the upper limit of bottom sediment resuspension.

attenuation coefficients by the water and suspended sediment, respectively. The calibration factors K_c and C' were determined by linear regression between acoustic backscatter and net volume scattering (Deines, 1999; Ha et al., 2011). This linear regression for acoustic signal calibration showed the reasonable correlation ($R^2 = 0.67$, Fig. 2), enabling inversion of ADCP backscatter intensity to SSC in this study.

3. Results

Time series collected from moorings M1 and M2 are presented in Figs. 3 and 4. During the observation periods at both sites, the water height showed typical semi-diurnal cycles with maximum tidal range of 9.28 m. The Sihwa TPP artificial discharge occurred only during ebb phase, and its volume varied over tidal cycles between spring and neap tides (Figs. 3a and 4a). During spring tides, the artificial discharge was much higher than during neap tides. It reached about 5.73×10^3 [7.79×10^3] $m^3\ s^{-1}$ during spring tides of M1 [M2], and dropped to about 0.72×10^3 [3.89×10^3] $m^3\ s^{-1}$ during neap tides. The mean wind stress over the entire measurement period of M1 [M2] was about 0.03 [0.02] Pa, exhibiting several peaks associated with episodic storm events. The storm events were exhibited during days 103.5–103.6 with maximum wind stress of 0.47 Pa. During these periods, the anthropogenic impacts for periodically high-concentration suspension was much greater than the wind impacts for that. Salinity changed with tidal phase, and intermittent drops and jumps were mainly associated with onsets and terminations of the artificial discharge. While freshwater was being released by artificial discharge, the M1 salinity decrement was less than 1.5 at the surface (21 mab) and that of M2 was less than 0.6 at the surface (12 mab) (Figs. 3c and 4c). Such different salinity responses are associated with the fact that the location of M1 is on the axis of the strong jet-flow, and M2 is slightly off the axis.

Along-channel velocity and ADCP-derived SSC (SSC_{ADCP}) exhibited a number of peaks associated with the periodic artificial discharge. Along-channel velocity peaks at M1 were positive with a maximum of $+1.04$ m s^{-1}, whereas those at M2 were negative with a maximum of -0.59 m s^{-1} (Figs. 3d and 4d). Along-channel velocity during spring tide was stronger than that during neap tide. Due to this strong along-channel jet-flow, SSC_{ADCP} during spring tide was much higher than that during neap tide (Figs. 3e and 4e). M1 and M2 maxima in SSC_{ADCP} were 1908.83 and 1149.30 mg l^{-1}, respectively. Details of vertical and temporal variations of SSC_{ADCP} are next examined for flood-ebb phases (Section 3.1) and spring-neap tidal cycles (Section 3.2).

3.1. SSC variation for flood and ebb phases

In order to investigate variations in SSC_{ADCP} and hydrodynamics

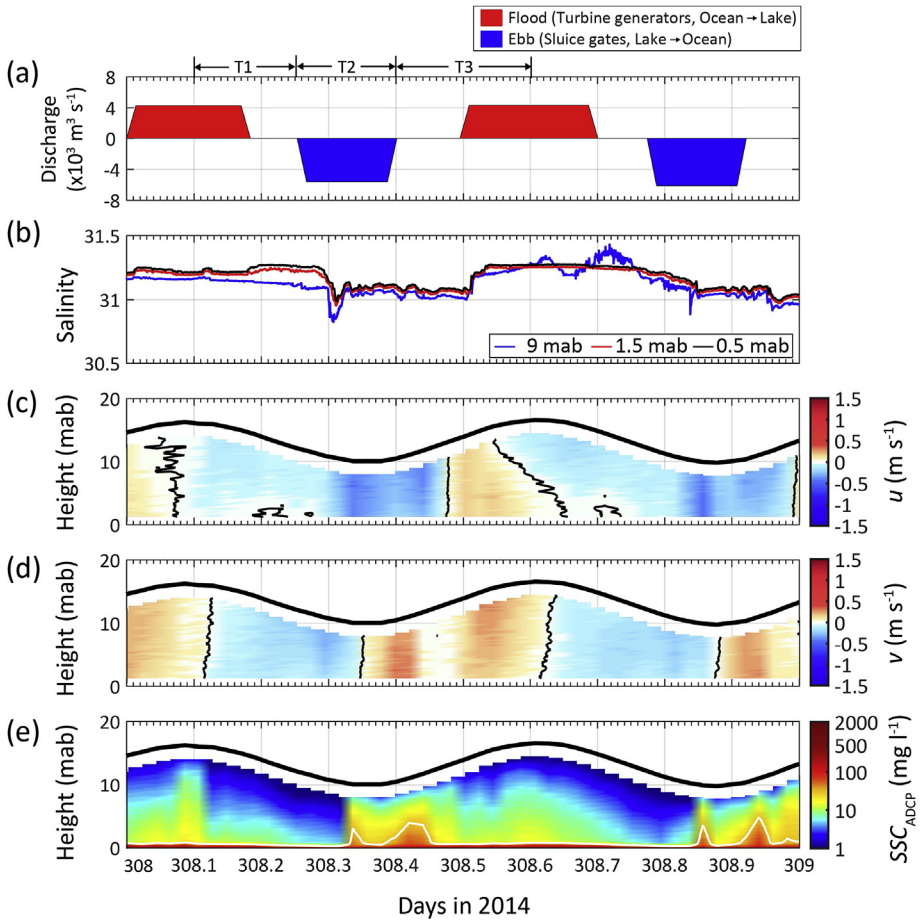


Fig. 6. Hydrodynamics and sediment dynamics at mooring M2 (for the selected time window, see Fig. 4): (a) discharge, (b) salinity, (c) along-channel velocity, (d) across-channel velocity, and (e) SSC_{ADCP}. Thick and thin black lines indicate water height (Fig. 6c, d and e) and zero velocity (Fig. 6c and d), respectively. The near-bed white line in Fig. 6e indicates 30 mg l^{-1}, used as the upper limit of bottom sediment resuspension.

for flood and ebb phases, two representative time windows (days 85–86 in Fig. 3; days 308–309 in Fig. 4) with similar artificial discharges are selectively examined in Figs. 5 and 6. During these periods, the artificial discharges of the TPP were about 5.57×10^3 m^3 s^{-1} and 5.63×10^3 m^3 s^{-1}, respectively. T1, T2 and T3 marked in Figs. 5 and 6 indicate the periods (i) before, (ii) during and (iii) after the artificial discharge, respectively.

During the T1 period (days 85.15–85.32 in Fig. 5) of M1, positive along- and across-channel velocities turned negative, with phase lags between them: near-surface (>17 mab) velocities turned negative earlier than those near the bed (<4 mab), and the duration of the positive across-channel velocity was 1 h longer than that of the positive along-channel velocity. Salinity near the surface (21 mab) remained almost constant (~29.82). High SSC_{ADCP} was confined to the near-bed layer.

During the T1 period (days 308.10–308.25 in Fig. 6) of M2, as with the M1 velocities, the duration of positive across-channel velocity was about 1 h longer than that of positive along-channel velocity, but the along- and across-channel velocities turned negative simultaneously through the entire water column on days 308.07 and 308.12, respectively. The salinities at 9, 1.5 and 0.5 mab remained almost constant (~31.14, 31.22 and 31.24), and the salinity difference between 9 and 0.5 mab was negligibly small (<0.1).

During the T2 period (days 85.32–85.49 in Fig. 5) of M1, there was a noticeable peak in SSC_{ADCP}. During days 85.32–85.35, the along-channel velocity turned from negative to positive at 17 mab, and the salinity rapidly decreased from 29.76 to 28.81. During days 85.35–85.42, velocity in the entire water column abruptly increased. The water was pushed seaward by the strong across-channel velocity (−1.51 m s^{-1}), and the resulting salinity at 21 mab quickly bounced back to 29.73. In addition, the increase in velocities induced by the discharge matched well with the increase in SSC_{ADCP}. During onset of the discharge, the bottom sediment was resuspended, and high SSC_{ADCP} extended upward into the water column above 10 mab (see the white line in Fig. 5e).

During the T2 period (days 308.25–308.40 in Fig. 6) of M2, there was a peak in SSC_{ADCP} associated with the negative along-channel velocity. When the negative along-channel velocity strengthened (~0.44 m s^{-1}) on day 308.33, the upper limit of bottom sediment resuspension reached up to 3 mab. The increase in SSC_{ADCP} at M1 was 1.5 times higher than that at M2. The salinity drops at M2 were affected by the across-channel velocity. When the positive across-channel velocity strengthened (~0.32 m s^{-1}) on day 308.3, the salinities at 9, 1.5 and 0.5 mab decreased from 31.08, 31.18 and 31.23 to 30.82, 30.95 and 30.98, respectively.

During the T3 period (days 85.49–85.65 in Fig. 5) of M1, three peaks in SSC_{ADCP} were observed on days 85.49, 85.53 and 85.60. The first and second peaks were associated with an increase in positive along-channel velocity with a maximum of 0.52 m s^{-1}. After day 85.56, the along-channel velocity showed a change of sign from

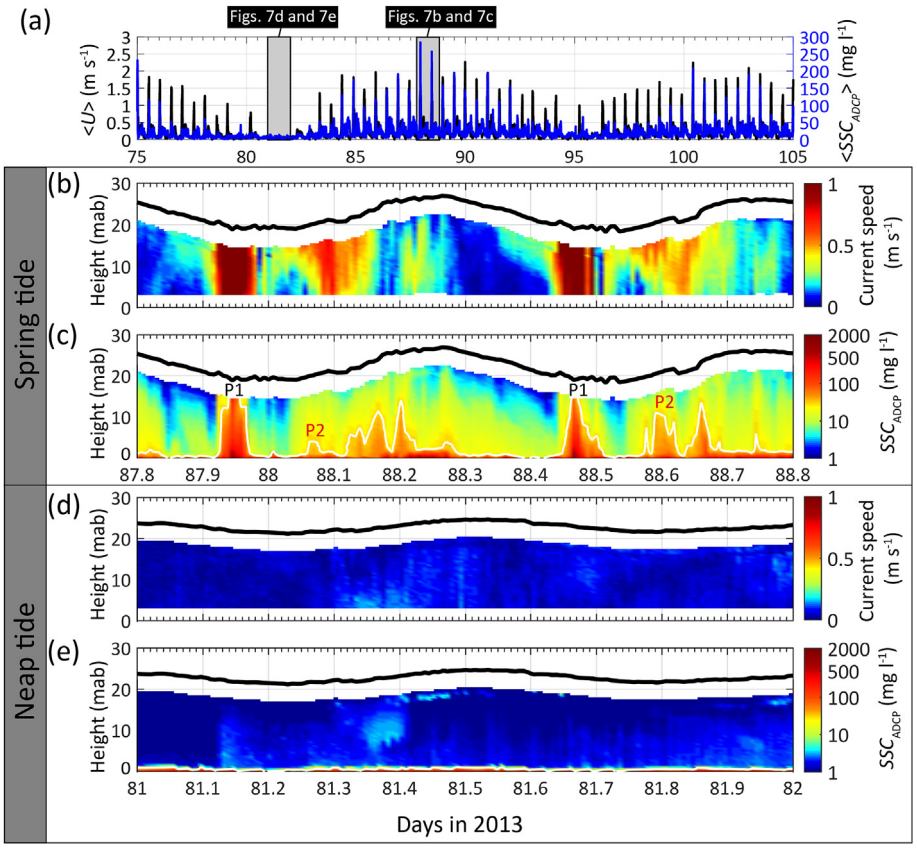


Fig. 7. Comparison of current speed and SSC_{ADCP} between spring and neap tides at mooring M1: (a) depth-averaged current speed (black line) and depth-averaged SSC_{ADCP} (blue line), (b) current speed and (c) SSC_{ADCP} during spring tide, (d) current speed and (e) SSC_{ADCP} during neap tide. Thick black lines indicate the water height. P1 and P2 represent the primary and secondary peaks in SSC_{ADCP}. Near-bed white lines in panels (c) and (e) indicate 30 mg l^{-1}, used as the upper limit of bottom sediment resuspension. (For interpretation of the references to colour in this figure legend, the reader is referred to the web version of this article.)

positive to negative, and SSC_{ADCP} increased again during days 85.56–85.60.

During the T3 period (days 308.40–308.60 in Fig. 6) of M2, a peak in SSC_{ADCP} was observed at 5 mab associated with positive across-channel velocity. When the positive across-channel velocity strengthened (~0.33 m s^{-1}) on day 308.42, the upper limit of bottom sediment resuspension reached up to 5 mab. When the positive across-channel velocity strengthened (~0.31 m s^{-1}) on day 308.55, salinities at 9, 1.5 and 0.5 mab increased to 31.23.

3.2. SSC variations by spring and neap tides

Profiles of depth-averaged SSC_{ADCP} ($\langle SSC_{ADCP}\rangle$) and depth-averaged current speed ($\langle U\rangle$) during spring and neap tides are shown in Figs. 7 and 8. Time series of $\langle SSC_{ADCP}\rangle$ at both sites exhibited significant differences between spring and neap tides. The selected data represent two periods having the highest difference (5.01×10^3 [3.90×10^3] m^3 s^{-1}) of artificial discharges between spring and neap tides.

At M1, $\langle SSC_{ADCP}\rangle$ had a maximum of 283.60 mg l^{-1} on day 87.94 during spring tide, and it decreased to 14.15 mg l^{-1} on day 81.10 during neap tide (Fig. 7a); $\langle U\rangle$ had a maximum of 2.36 m s^{-1} during spring tide (day 87.94), and was 0.10 m s^{-1} during neap tide (day 81.49). The peaks of $\langle U\rangle$ during spring tide exhibited good correspondence with the peaks of $\langle SSC_{ADCP}\rangle$. At M2, $\langle SSC_{ADCP}\rangle$ had a maximum of 43.87 mg l^{-1} on day 313.60 during spring tide, and it decreased to 23.89 mg l^{-1} on day 318.10 during neap tide (Fig. 8a); $\langle U\rangle$ had a maximum of 0.71 m s^{-1} during spring tide (day 313.40), and was 0.38 m s^{-1} during neap tide (day 318.10).

At M1, mean SSC_{ADCP} during spring tide was approximately 5 times higher than that during neap tide (Table 1). During spring tide, the mean current speed and SSC_{ADCP} were respectively about 0.36 m s^{-1} and 27.93 mg l^{-1} (Fig. 7b and c), whereas they were about 0.05 m s^{-1} and 5.73 mg l^{-1} during neap tide (Fig. 7d and e). During artificial discharge, current speed peaks (>2 m s^{-1}) accordingly matched with SSC_{ADCP} peaks during spring tide, and the resuspension of high SSC layer reached near the water surface ("P1" in Fig. 7c). In contrast, the SSC_{ADCP} during neap tide was fairly low (<5 mg l^{-1}) throughout the entire water column, and the high SSC layer was only observed near the bed, forming a thin fluffy layer (Fig. 7e).

At M2, mean SSC_{ADCP} during spring tide was approximately double that during neap tide (Table 1). During spring tide, mean current speed and SSC_{ADCP} were respectively about 0.28 m s^{-1} and 25.77 mg l^{-1}, whereas they were about 0.14 m s^{-1} and 13.46 mg l^{-1} during neap tide (Fig. 8). Double peaks in current speed during spring tide were associated with double peaks in SSC_{ADCP} during days 313.42–313.58 (Fig. 8b and c), and the high SSC layer reached to 3–4 mab. As at M1, the high SSC layer at M2 during neap tide was observed only near the bed (Fig. 8e).

4. Discussion

Unlike those in natural tidal environments, hydrodynamics and

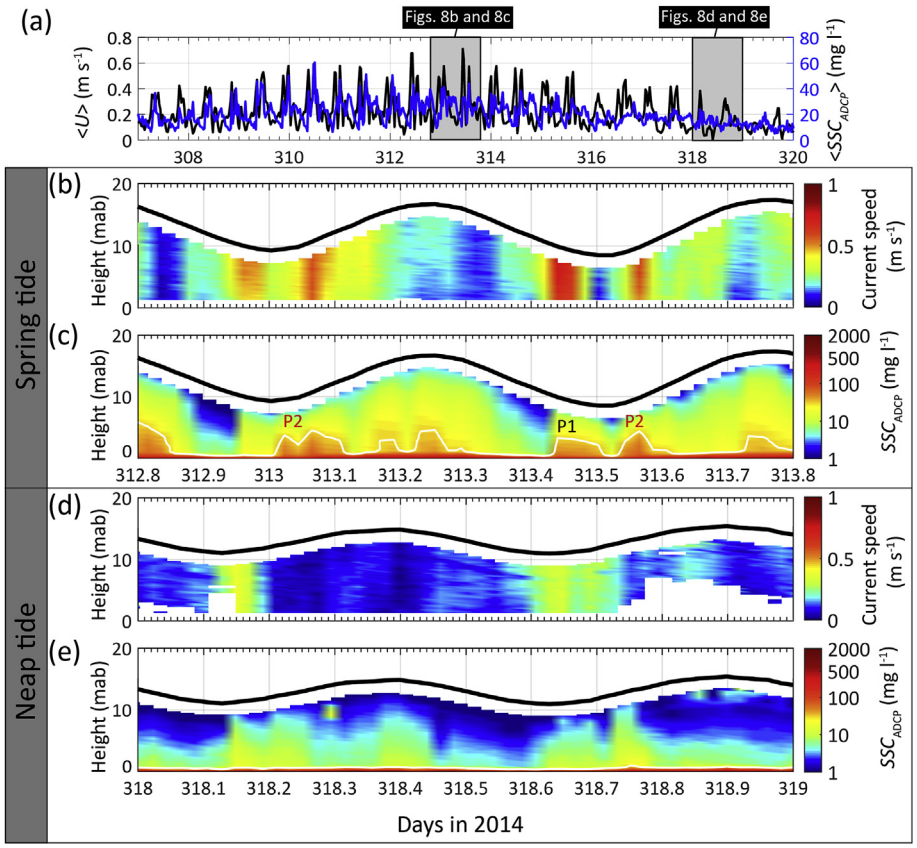


Fig. 8. Comparison of current speed and SSC_{ADCP} between spring and neap tides at mooring M2: (a) depth-averaged current speed (black line) and depth-averaged SSC_{ADCP} (blue line), (b) current speed and (c) SSC_{ADCP} during spring tide, (d) current speed and (e) SSC_{ADCP} during neap tide. Thick black lines indicate the water height. P1 and P2 represent the primary and secondary peaks in SSC_{ADCP}. Near-bed white lines in panels (c) and (e) indicate 30 mg l^{-1}, used as the upper limit of bottom sediment resuspension. (For interpretation of the references to colour in this figure legend, the reader is referred to the web version of this article.)

sediment transport in the vicinity of the Sihwa area are overwhelmed by the periodic artificial discharge. The disturbance of sediment dynamics in response to anthropogenic activities has been reported in tidal energy barrages such as La Rance (France) and Annapolis Royal (Canada) TPPs (Kirby and Retière, 2009; Morris, 2013). After construction and operation, most TPPs experience a reduction of current speed, resulting in a significant decrease in SSC (Kirby and Retière, 2009; Ahmadian and Falconer, 2012; Ahmadian et al., 2014). For instance, La Rance has a change in erosion patterns due to the reduction in tidal range with loss of intertidal area. Blocking of water flow by the dam in Annapolis Royal allowed sediment to settle to the bed, leading to increased river bank erosion at both the upstream and downstream ends (Morris, 2013). The Sihwa area also has noticeable sediment issues related to the strong jet-flow during the discharge period. However, it differs significantly from the aforementioned TPPs in that the discharge direction is oblique to the main passage of flood-ebb tides along funnel-shape estuaries, and the discharge velocity (>2 m s^{-1}) is much higher than the background level of tidal currents prior to the operation. Details on how the Sihwa TPP is significantly disturbing the sediment transport are discussed below.

Fig. 9 shows the characteristic responses, at moorings M1 and M2, to TPP operation over tidal cycles. During the first hour (indicated as "S1") after the start of artificial discharge, the relationship between $<SSC_{ADCP}>$ and $<U>$ at both mooring sites is poor (R^2<0.28 [0.10]). During the next hour after S1 (indicated as "S2"), the strong current associated with the artificial discharge eroded bed sediment and maintained a large amount of sediment in suspension up to the surface layer. $<SSC_{ADCP}>$ at M1 started to increase abruptly when $<U>$ exceeded about 1 m s^{-1}, indicating the existence of a critical velocity for erosion (or resuspension). The correlation becomes higher (R^2 = 0.68 for $<U>$ >1 m s^{-1}), and maximum $<SSC_{ADCP}>$ of 283.61 mg l^{-1} was observed at M1 (Fig. 9a). This response suggests that the most active suspension of bed sediment occurred during 1–2 h immediately after the start of artificial discharge (see "P1" in Figs. 7c, 8c and 9b and 9d). Considering the artificial-discharge travel time from the sluice gates to mooring M1, a certain response time (i.e., 1–2 h) is required to increase SSC by local resuspension as well as advection of the discharge-derived, high-concentration flow. While $<U>$ at M2 during the S2 period reached 0.7 m s^{-1}, $<SSC_{ADCP}>$ increased only to 36.62 mg l^{-1} (Fig. 9c). When the stage turned to the S3 period (the time remaining to the end of artificial discharge), $<SSC_{ADCP}>$ at M1 quickly dropped below 50 mg l^{-1}. Because the S3 period included a tidal slack, the suspended sediment could settle down into the bed layer. However, $<SSC_{ADCP}>$ at M2 during the S3 period remained almost the same as $<SSC_{ADCP}>$ during the previous time window (S2). During the first hour ("E1") after the end of artificial discharge, $<U>$ at M1 decreased to almost half of velocities observed during the S3 period, but $<SSC_{ADCP}>$ increased slightly to 65.47 mg l^{-1}, producing a secondary SSC peak (see "P2" in Figs. 7c, 8c and 9b and 9d). Similarly, $<SSC_{ADCP}>$ at M2 during the E1 period also increased to 57.84 mg l^{-1}, which is the maximum SSC measured at M2. For the sediment volume entering and leaving

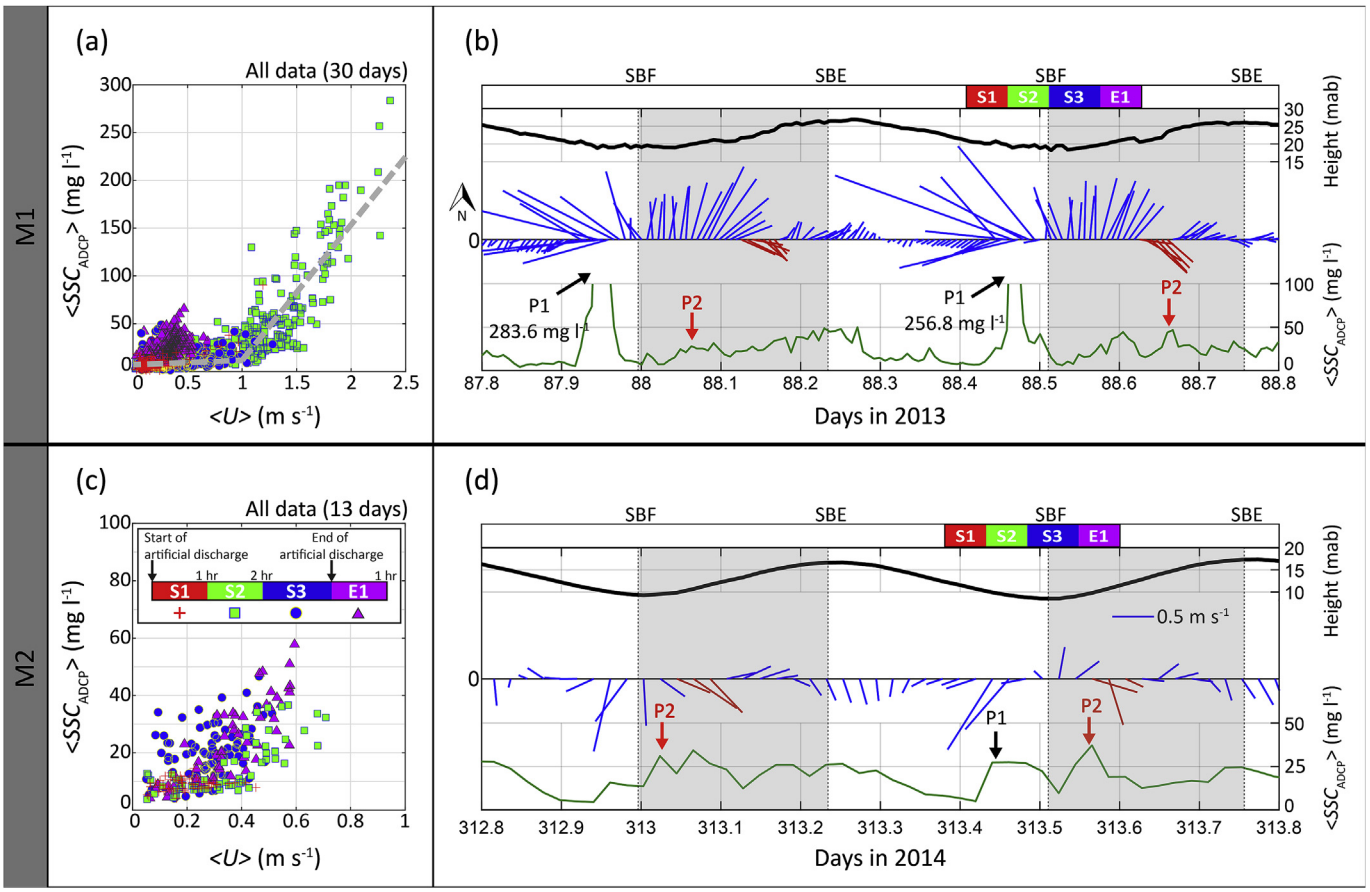


Fig. 9. (a, c) Relationships between depth-averaged SSC_{ADCP} ($<SSC_{ADCP}>$) and depth-averaged current speed ($<U>$) at moorings M1 and M2. Labels (S1, S2, S3 and E1) represent four time windows before (S1–S3) and after (E1) the artificial discharge. Grey dashed line in Fig. 9a indicates an interpreted line ($R^2 = 0.68$ for $<U> > 1$ m s^{-1}) to define a critical velocity for erosion. (b, d) Representative time series of mooring data varied by the artificial discharge and tidal cycles. Thick black lines indicate water height, and red sticks indicate southeastward flows associated with the anticlockwise rotating vortex after turning to flood phase. SBF and SBE represent tidal slacks before flood and ebb, respectively. P1 and P2 represent the primary and secondary peaks in SSC_{ADCP}. Note that the ranges of *x*- and *y*-axes for the two moorings are different. (For interpretation of the references to colour in this figure legend, the reader is referred to the web version of this article.)

Sihwa TPP, the asymmetric peaks in $<SSC_{ADCP}>$ at "P1" and "P2" contribute to the increase of sediment volume in the seaward direction rather than that in the landward direction. In the view of the long-term sedimentation, therefore, it is expected that the seaward net sediment volume might cause the reduction of intertidal zone and wetland maintenance problems in upstream area.

During the E1 period (flood phase), southeastward flows (see red sticks in Fig. 9b and d) were predominately observed. Also, secondary peaks in $<SSC_{ADCP}>$ were detected, since a weak current can readily resuspend near-bed sediment which was not fully consolidated during the previous slack due to insufficient time (Ha and Maa, 2009). Possible reasons why mooring M2 shows the highest SSC during E1 rather than S2, are that the site is not directly facing the artificial discharge expelled through the sluice gates, and that an anticlockwise rotating vortex induces sediment transport toward the Sihwa TPP (southeastward). Wells and van Heijst (2003) claimed that strong jet-flow through a narrow inlet channel forms a dipole structure of tidal vortices. In this study, however, the dipole feature is not fully developed in front of the Sihwa TPP, because strong ebb currents obstruct formation of the clockwise rotating vortex, but reinforce formation of the anticlockwise rotating vortex produced by the horizontal velocity shear (Kim et al., 2009). Secondary peaks in SSC at moorings M1 and M2 during the flood phase can be explained by the existence of the anticlockwise rotating vortex.

In summary, the schematic mechanisms for sediment transport in the vicinity of the Sihwa TPP are presented in Fig. 10. Current velocities at moorings M1 and M2 dominated the discharge-induced northwestward (or westward) flow during ebb phase (Fig. 10a). The flow at M1 began to be deflected by the strong ebb current, forming an anticlockwise rotating vortex. During this period, suspension of bed sediment occurred strongly at M1. At the slack before flood (Fig. 10b), the transport direction of suspended sediment shifted to that of the northwestward flow, and the SSC slightly decreased. While the tide was turning to flood phase and the artificial discharge was still in progress, the vortex core migrated northeastward (Fig. 10c). During mid-flood tides without artificial discharge, velocities at M1 and M2 rapidly changed to southeastward flows (Fig. 10d) due to full development of the vortex. Flow toward the turbine generators during flood phase could also contribute to intensification of the southeastward flow and sediment transport.

5. Conclusions

Observations with surface moorings have been conducted at the Sihwa TPP, the world's largest, to understand the hydrodynamics and sediment dynamics disturbed by anthropogenic impacts. The following conclusions are drawn from this study:

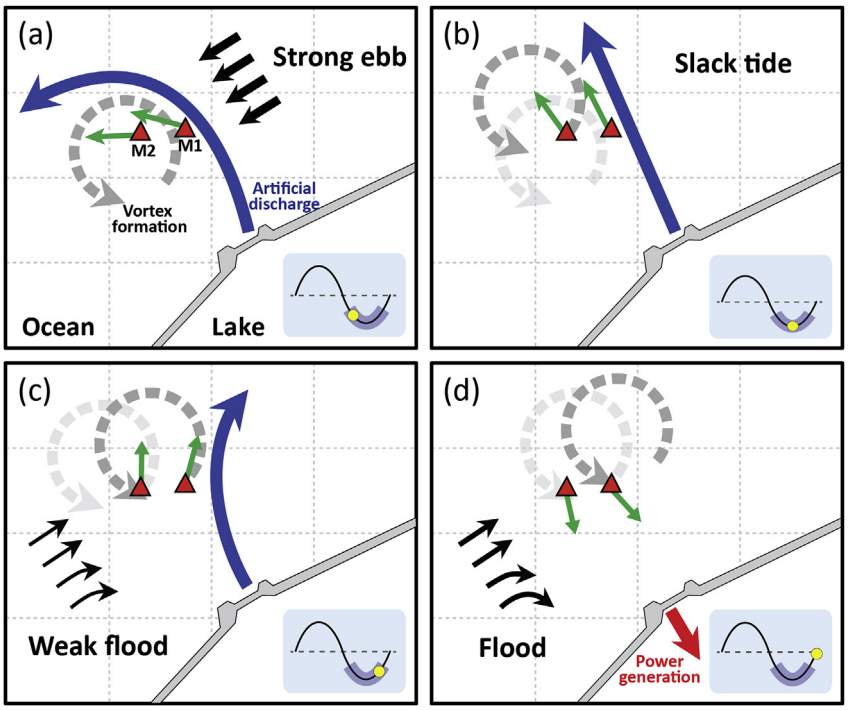


Fig. 10. Schematic mechanisms for explaining the anticlockwise rotating vortex and associated sediment transport: (a) strong ebb, (b) slack before flood, (c) beginning of flood, and (d) mid-flood phases (for corresponding tidal phases, see yellow dots in the insets). Blue, red and black arrows indicate simplified flow patterns generated by the artificial discharge, power generation and tides, respectively. Green arrows represent the prevailing direction of sediment transport at the mooring stations. Dark and light grey dashed circles with arrows show respectively the location of the anticlockwise rotating vortex in present and previous time steps. (For interpretation of the references to colour in this figure legend, the reader is referred to the web version of this article.)

(1) Strong jet-flow (>2 m s^{-1}) and resulting anticlockwise rotating vortex, showing great variability in response to the artificial discharge, are key controlling factors in eroding the bed sediment and maintaining it in suspension.
(2) In the area directly facing the artificial discharge (mooring M1), the most active suspension of bed sediment predominantly occurred during 1–2 h immediately after the start of discharge. The increments in the depth-averaged current and SSC at M1 were about 1.5 m s^{-1} and 200 mg l^{-1}. Meanwhile, in the area away from the artificial discharge (mooring M2), SSC increased immediately after the start of discharge, and the highest SSC at M2 was observed immediately after the end of discharge. The increments in the depth-averaged current and SSC at M2 were about 0.3 m s^{-1} and 25 mg l^{-1}.
(3) During ebb phase, the strong jet-flow moved the suspended sediment seaward. After turning to flood phase, the fully developed anticlockwise rotating vortex induced southeastward flows, transporting the suspended sediment toward the Sihwa TPP.
(4) SSC during spring tide was approximately 2–5 times higher than during neap tide. During the combined period of ebb and spring tides, in particular, the periodic artificial discharge can enhance the responses of SSC in the vicinity of Sihwa TPP.

Acknowledgments

This research was a part of the project titled 'Gyeonggi Sea Grant Program', funded by the Ministry of Oceans and Fisheries, Korea (20140241). HKH was supported by the National Research Foundation of Korea (NRF-2015R1D1A1A01057726). S.M. Choi helped to prepare the graphics.

References

Ahmadian, R., Falconer, R.A., 2012. Assessment of array shape of tidal stream turbines on hydro-environmental impacts and power output. Renew. Energy 44, 318–327.
Ahmadian, R., Falconer, R.A., Bockelmann-Evans, B., 2014. Comparison of hydro-environmental impacts for ebb-only and two-way generation for a Severn Barrage. Comput. Geosci. 71, 11–19.
Angeloudis, A., Falconer, R.A., 2017. Sensitivity of tidal lagoon and barrage hydrodynamic impacts and energy outputs to operational characteristics. Renew. Energy (in press). http://dx.doi.org/10.1016/j.renene.2016.08.033.
Bae, Y.H., Kim, K.O., Choi, B.H., 2010. Lake Sihwa tidal power plant project. Ocean. Eng. 37, 454–463.
Baek, S.H., Ki, J.S., Katano, T., You, K., Park, B.S., Shin, H.H., Shin, K., Kim, Y.O., Han, M.S., 2011. Dense winter bloom of the dinoflagellate Heterocapsa triquetra below the thick surface ice of brackish Lake Shihwa, Korea. Phycol. Res. 59, 273–285.
Charlier, R.H., Finkl, C.W., 2009. Ocean Energy: Tide and Tidal Power. Springer–Verlag, Berlin Heidelberg, 262 pp.
Choi, M., Furlong, E.T., Moon, H., Yu, J., Choi, H., 2011. Contamination of nonylphenolic compounds in creek water, wastewater treatment plant effluents, and sediments from Lake Shihwa and vicinity, Korea: comparison with fecal pollution. Chemosphere 85, 1406–1413.
Deines, K.L., 1999. Backscatter estimation using broadband acoustic Doppler current profilers. In: Proceedings of the 6th IEEE Working Conference on Current Measurement. San Diego, CA, pp. 249–253.
Ha, H.K., Maa, J.P.-Y., 2009. Evaluation of two conflicting paradigms for cohesive sediment deposition. Mar. Geol. 265, 120–129.
Ha, H.K., Maa, J.P.-Y., Park, K., Kim, Y.H., 2011. Estimation of high-resolution sediment concentration profiles in bottom boundary layer using pulse-coherent acoustic Doppler current profilers. Mar. Geol. 279, 199–209.
Han, M.W., Park, Y.C., 1999. The development of anoxia in the artificial Lake Shihwa, Korea, as a consequence of intertidal reclamation. Mar. Pollut. Bull. 38, 1194–1199.
Kang, N.S., Lee, K.H., Jeong, H.J., Yoo, Y.D., Seong, K.A., Potvin, E., Hwang, Y.J., Yoon, E.Y., 2013. Red tides in Shiwha Bay, western Korea: a huge dike and tidal power plant established in a semi-closed embayment system. Harmful Algae 30, 114–130.
Khim, J.S., Villeneuve, D.L., Kannan, K., Lee, K.T., Snyder, S.A., Koh, C.H., Giesy, J.P., 1999. Alkylphenols, polycyclic aromatic hydrocarbons, and organochlorines in sediment from Lake Shihwa, Korea: instrumental and bioanalytical characterization. Environ. Toxicol. Chem. 18, 2424–2432.

Kim, D.-H., Lynett, P.J., Socolofsky, S.A., 2009. A depth-integrated model for weakly dispersive, turbulent, and rotational fluid flows. Ocean. Model. 27, 198–214.
Kirby, R., Retière, C., 2009. Comparing environmental effects of Rance and Severn barrages. Marit. Eng. 162, 11–26.
Kirby, R., 2010. Distribution, transport and exchanges of fine sediment, with tidal power implications: Severn Estuary, UK. Mar. Pollut. Bull. 61, 21–36.
Lee, C.H., Lee, B.-Y., Chang, W.K., Hong, S., Song, S.J., Park, J., Kwon, B.-O., Khim, J.S., 2014. Environmental and ecological effects of Lake Shihwa reclamation project in South Korea: a review. Ocean Coast. Manag. 102, 545–558.
Li, D., Kim, M., Oh, J.R., Park, J., 2004. Distribution characteristics of nonylphenols in the artificial Lake Sihwa, and surrounding creeks in Korea. Chemosphere 56, 783–790.
Morris, R.K.A., 2013. Geomorphological analogues for large estuarine engineering projects: a case study of barrages, causeways and tidal energy projects. Ocean Coast. Manag. 79, 52–61.
Neill, S.P., Jordan, J.R., Couch, S.J., 2012. Impact of tidal energy converter (TEC) arrays on the dynamics of headland sand banks. Renew. Energy 37, 387–397.
Oh, S., Kim, M.K., Yi, S.M., Zoh, K.D., 2010. Distribution of total mercury and methylmercury in surface sediments and fishes in Lake Shihwa, Korea. Sci. Total Environ. 408, 1059–1068.
Ra, K., Bang, J., Lee, J., Kim, K., Kim, E., 2011. The extent and historical trend of metal pollution recorded in core sediments from the artificial Lake Shihwa, Korea. Mar. Pollut. Bull. 62, 1814–1821.
Ramos, V., Carballo, R., Sánchez, M., Veigas, M., Iglesias, G., 2014. Tidal stream energy impacts on estuarine circulation. Energy Convers. Manag. 80, 137–149.
Rostkowski, P., Yamashita, N., So, I.M.K., Taniyasu, S., Lam, P.K.S., Falandysz, J., Lee, K.T., Kim, S.K., Khim, J.S., Im, S.H., Newsted, J.L., Jones, P.D., Kannan, K., Giesy, J.P., 2006. Perfluorinated compounds in streams of the Shihwa industrial zone and Lake Shihwa, South Korea. Environ. Toxicol. Chem. 25, 2374–2380.
Rourke, F.O., Boyle, F., Reynolds, A., 2010a. Tidal energy update 2009. Appl. Energy 87, 398–409.
Rourke, F.O., Boyle, F., Reynolds, A., 2010b. Marine current energy devices: current status and possible future applications in Ireland. Renew. Sustain. Energy Rev. 14, 1026–1036.
Susaya, J., Kim, K.H., Chang, Y.S., 2011. Characterization of major offensive odorants released from lake sediment. Atmos. Environ. 45, 1236–1241.
Tolón-Becerra, A., Lastra-Bravo, X., Bienvenido-Barcena, F., 2011. Proposal for territorial distribution of the EU 2020 political renewable energy goal. Renew. Energy 36, 2067–2077.
Wells, M.G., van Heijst, G.-J.F., 2003. A model of tidal flushing of an estuary by dipole formation. Dyn. Atmos. Oceans 37, 223–244.
Wu, J., 1980. Wind-stress coefficients over sea surface near neutral conditions–a revisit. J. Phys. Oceanogr. 10, 727–740.
Xia, J., Falconer, R.A., Lin, B., 2010. Impact of different operating modes for a Severn Barrage on the tidal power and flood inundation in the Severn Estuary, UK. Appl. Energy 87, 2374–2391.
Yoo, H., Kannan, K., Kim, S.K., Lee, K.T., Newsted, J.L., Giesy, J.P., 2008. Perfluoroalkyl acids in the egg yolk of birds from Lake Shihwa, Korea. Environ. Sci. Technol. 42, 5821–5827.
Zhou, J., Falconer, R.A., Lin, B., 2014. Refinements to the EFDC model for predicting the hydro-environmental impacts of a barrage across the Severn Estuary. Renew. Energy 62, 490–505.